Research Article | Vol. 8, No. 3 | 1 Mar 2017 | BIOMEDICAL OPTICS EXPRESS 1372
Biomedical Optics EXPRESS

Dermoscopy guided dark-field multi-functional optical coherence tomography

SOONJAE KWON,[1,5] YEOREUM YOON,[1,5] BUMJU KIM,[2] WON HYUK JANG,[2] BYUNGHO OH,[3] KEE YANG CHUNG,[4,6] AND KI HEAN KIM[1,2,7]

[1]*Department of Mechanical Engineering, Pohang University of Science and Technology, San 31, Hyoja-dong, Nam-gu, Pohang, Gyeongbuk 790-784, South Korea*
[2]*Division of Integrative Biosciences and Biotechnology, Pohang University of Science and Technology, San 31, Hyoja-dong, Nam-gu, Pohang, Gyeongbuk 790-784, South Korea*
[3]*Department of Dermatology, Keimyung University, College of Medicine, 56, Dalseong-ro, Jung-gu, Daegu, 41931, South Korea*
[4]*Departments of Dermatology, Severance Hospital, Cutaneous Biology Research Institute, Yonsei University College of Medicine, Seoul, 03722, South Korea*
[5]*These authors contributed equally to this work*
[6]*kychung@yuhs.ac*
[7]*kiheankim@postech.ac.kr*

Abstract: Dermoscopy is a skin surface microscopic technique allowing specular reflection free observation of the skin, and has been used to examine pigmented skin lesions. However, dermoscopy has limitations in providing depth information due to lack of 3D resolution. In order to overcome the limitations, we developed dermoscopy guided multi-functional optical coherence tomography (MF-OCT) providing both high-contrast superficial information and depth-resolved structural, birefringent, and vascular information of the skin simultaneously. Dermoscopy and MF-OCT were combined by using a dichroic mirror, and dark-field configuration was adapted for MF-OCT to reduce specular reflection. After characterization, dermoscopy guided MF-OCT was applied to several human skin lesions such as the scar, port-wine stain (PWS) as well as the normal skin for demonstration. Various features of the scar and PWS were elucidated by both dermoscopy and MF-OCT. Dermoscopy guided MF-OCT may be useful for evaluation and treatment monitoring of skin lesions in clinical applications.

OCIS codes: (170.4500) Optical coherence tomography; (170.1870) Dermatology; (130.5440) Polarization-selective devices; (170.0170) Medical optics and biotechnology.

References and links

1. M. E. Vestergaard, P. Macaskill, P. E. Holt, and S. W. Menzies, "Dermoscopy compared with naked eye examination for the diagnosis of primary melanoma: a meta-analysis of studies performed in a clinical setting," Br. J. Dermatol. **159**(3), 669–676 (2008).
2. G. Argenziano and H. P. Soyer, "Dermoscopy of pigmented skin lesions–a valuable tool for early," Lancet Oncol. **2**(7), 443–449 (2001).
3. R. P. Braun, H. S. Rabinovitz, M. Oliviero, A. W. Kopf, and J.-H. Saurat, "Dermoscopy of pigmented skin lesions," J. Am. Acad. Dermatol. **52**(1), 109–121 (2005).
4. M.-L. Bafounta, A. Beauchet, P. Aegerter, and P. Saiag, "Is dermoscopy (epiluminescence microscopy) useful for the diagnosis of melanoma? Results of a meta-analysis using techniques adapted to the evaluation of diagnostic tests," Arch. Dermatol. **137**(10), 1343–1350 (2001).
5. I. Zalaudek, J. Kreusch, J. Giacomel, G. Ferrara, C. Catricalà, and G. Argenziano, "How to diagnose nonpigmented skin tumors: a review of vascular structures seen with dermoscopy: part I. Melanocytic skin tumors," J. Am. Acad. Dermatol. **63**(3), 361–374 (2010).
6. I. Zalaudek, G. Argenziano, B. Leinweber, L. Citarella, R. Hofmann-Wellenhof, J. Malvehy, S. Puig, M. A. Pizzichetta, L. Thomas, H. P. Soyer, and H. Kerl, "Dermoscopy of Bowen's disease," Br. J. Dermatol. **150**(6), 1112–1116 (2004).
7. I. Zalaudek, "Dermoscopy subpatterns of nonpigmented skin tumors," Arch. Dermatol. **141**(4), 532 (2005).
8. A. Lallas, J. Giacomel, G. Argenziano, B. García-García, D. González-Fernández, I. Zalaudek, and F. Vázquez-López, "Dermoscopy in general dermatology: practical tips for the clinician," Br. J. Dermatol. **170**(3), 514–526 (2014).

#281436 https://doi.org/10.1364/BOE.8.001372
Journal © 2017 Received 23 Nov 2016; revised 31 Jan 2017; accepted 31 Jan 2017; published 6 Feb 2017

Biomedical Optics EXPRESS

9. M. Shirakawa, T. Ozawa, S. Wakami, M. Ishii, and T. Harada, "Utility of dermoscopy before and after laser irradiation in port wine stains," Ann. Dermatol. **24**(1), 7–10 (2012).
10. T. Micantonio, M. C. Fargnoli, and K. Peris, "Usefulness of dermoscopy to monitor clinical efficacy of imiquimod treatment for lentigo maligna," Arch. Dermatol. **142**(4), 523–531 (2006).
11. D. Huang, E. A. Swanson, C. P. Lin, J. S. Schuman, W. G. Stinson, W. Chang, M. R. Hee, T. Flotte, K. Gregory, and C. A.Puliafito, "Optical coherence tomography," Science **254**(5035), 1178–1181 (1991).
12. J. Welzel, E. Lankenau, R. Birngruber, and R. Engelhardt, "Optical coherence tomography of the human skin," J. Am. Acad. Dermatol. **37**(6), 958–963 (1997).
13. M. Mogensen, L. Thrane, T. M. Jørgensen, P. E. Andersen, and G. B. Jemec, "OCT imaging of skin cancer and other dermatological diseases," J. Biophotonics **2**(6-7), 442–451 (2009).
14. J. Welzel, "Optical coherence tomography in dermatology: a review," Skin Res. Technol. **7**(1), 1–9 (2001).
15. T. Gambichler, G. Moussa, M. Sand, D. Sand, P. Altmeyer, and K. Hoffmann, "Applications of optical coherence tomography in dermatology," J. Dermatol. Sci. **40**(2), 85–94 (2005).
16. E. Götzinger, M. Pircher, W. Geitzenauer, C. Ahlers, B. Baumann, S. Michels, U. Schmidt-Erfurth, and C. K. Hitzenberger, "Retinal pigment epithelium segmentation by polarization sensitive optical coherence tomography," Opt. Express **16**(21), 16410–16422 (2008).
17. M. C. Pierce, R. L. Sheridan, B. H. Park, B. Cense, and J. F. de Boer, "Collagen denaturation can be quantified in burned human skin using polarization-sensitive optical coherence tomography," Burns **30**(6), 511–517 (2004).
18. C. E. Saxer, J. F. de Boer, B. H. Park, Y. Zhao, Z. Chen, and J. S. Nelson, "High-speed fiber based polarization-sensitive optical coherence tomography of in vivo human skin," Opt. Lett. **25**(18), 1355–1357 (2000).
19. K. H. Kim, M. C. Pierce, G. Maguluri, B. H. Park, S. J. Yoon, M. Lydon, R. Sheridan, and J. F. de Boer, "In vivo imaging of human burn injuries with polarization-sensitive optical coherence tomography," J. Biomed. Opt. **17**(6), 066012 (2012).
20. W.-C. Kuo, N.-K. Chou, C. Chou, C.-M. Lai, H.-J. Huang, S.-S. Wang, and J.-J. Shyu, "Polarization-sensitive optical coherence tomography for imaging human atherosclerosis," Appl. Opt. **46**(13), 2520–2527 (2007).
21. Y. Yasuno, S. Makita, Y. Sutoh, M. Itoh, and T. Yatagai, "Birefringence imaging of human skin by polarization-sensitive spectral interferometric optical coherence tomography," Opt. Lett. **27**(20), 1803–1805 (2002).
22. S. M. Srinivas, J. F. de Boer, H. Park, K. Keikhanzadeh, H. E. Huang, J. Zhang, W. Q. Jung, Z. Chen, and J. S. Nelson, "Determination of burn depth by polarization-sensitive optical coherence tomography," J. Biomed. Opt. **9**(1), 207–212 (2004).
23. W. C. Lo, M. Villiger, A. Golberg, G. F. Broelsch, S. Khan, C. G. Lian, W. G. Austen, Jr., M. Yarmush, and B. E. Bouma, "Longitudinal, 3D Imaging of Collagen Remodeling in Murine Hypertrophic Scars In Vivo Using Polarization-Sensitive Optical Frequency Domain Imaging," J. Invest. Dermatol. **136**(1), 84–92 (2016).
24. A. Latrive, L. R. Teixeira, A. S. Gomes, and D. M. Zezell, "Characterization of skin Port-Wine Stain and Hemangioma vascular lesions using Doppler OCT," Skin Res. Technol. **22**(2), 223–229 (2016).
25. C. Blatter, J. Weingast, A. Alex, B. Grajciar, W. Wieser, W. Drexler, R. Huber, and R. A. Leitgeb, "In situ structural and microangiographic assessment of human skin lesions with high-speed OCT," Biomed. Opt. Express **3**(10), 2636–2646 (2012).
26. G. Liu, W. Jia, J. S. Nelson, and Z. Chen, "In vivo, high-resolution, three-dimensional imaging of port wine stain microvasculature in human skin," Lasers Surg. Med. **45**(10), 628–632 (2013).
27. M. Ulrich, T. von Braunmuehl, H. Kurzen, T. Dirschka, C. Kellner, E. Sattler, C. Berking, J. Welzel, and U. Reinhold, "The sensitivity and specificity of optical coherence tomography for the assisted diagnosis of nonpigmented basal cell carcinoma: an observational study," Br. J. Dermatol. **173**(2), 428–435 (2015).
28. A. J. Coleman, G. P. Penney, T. J. Richardson, A. Guyot, M. J. Choi, N. Sheth, E. Craythorne, A. Robson, and R. Mallipeddi, "Automated registration of optical coherence tomography and dermoscopy in the assessment of sub-clinical spread in basal cell carcinoma," Comput. Aided Surg. **19**(1-3), 1–12 (2014).
29. R. Dsouza, H. Subhash, K. Neuhaus, J. Hogan, C. Wilson, and M. Leahy, "Dermascope guided multiple reference optical coherence tomography," Biomed. Opt. Express **5**(9), 2870–2882 (2014).
30. M. Villiger, C. Pache, and T. Lasser, "Dark-field optical coherence microscopy," Opt. Lett. **35**(20), 3489–3491 (2010).
31. Y. Yoon, Q. Li, V. H. Le, W. H. Jang, T. Wang, B. Kim, S. Son, W. K. Chung, C. Joo, and K. H. Kim, "Dark-field polarization-sensitive optical coherence tomography," Opt. Express **23**(10), 12874–12886 (2015).
32. C. Blatter, B. Grajciar, C. M. Eigenwillig, W. Wieser, B. R. Biedermann, R. Huber, and R. A. Leitgeb, "Extended focus high-speed swept source OCT with self-reconstructive illumination," Opt. Express **19**(13), 12141–12155 (2011).
33. R. A. Leitgeb, M. Villiger, A. H. Bachmann, L. Steinmann, and T. Lasser, "Extended focus depth for Fourier domain optical coherence microscopy," Opt. Lett. **31**(16), 2450–2452 (2006).
34. X. Yu, X. Liu, J. Gu, D. Cui, J. Wu, and L. Liu, "Depth extension and sidelobe suppression in optical coherence tomography using pupil filters," Opt. Express **22**(22), 26956–26966 (2014).
35. Y. Lim, Y.-J. Hong, L. Duan, M. Yamanari, and Y. Yasuno, "Passive component based multifunctional Jones matrix swept source optical coherence tomography for Doppler and polarization imaging," Opt. Lett. **37**(11), 1958–1960 (2012).
36. B. Baumann, W. Choi, B. Potsaid, D. Huang, J. S. Duker, and J. G. Fujimoto, "Swept source/Fourier domain polarization sensitive optical coherence tomography with a passive polarization delay unit," Opt. Express **20**(9), 10229–10241 (2012).

Biomedical Optics EXPRESS

37. B. Cense, N. Nassif, T. Chen, M. Pierce, S.-H. Yun, B. Park, B. Bouma, G. Tearney, and J. de Boer, "Ultrahigh-resolution high-speed retinal imaging using spectral-domain optical coherence tomography," Opt. Express **12**(11), 2435–2447 (2004).
38. M. Wojtkowski, V. Srinivasan, T. Ko, J. Fujimoto, A. Kowalczyk, and J. Duker, "Ultrahigh-resolution, high-speed, Fourier domain optical coherence tomography and methods for dispersion compensation," Opt. Express **12**(11), 2404–2422 (2004).
39. K. H. Kim, B. H. Park, Y. Tu, T. Hasan, B. Lee, J. Li, and J. F. de Boer, "Polarization-sensitive optical frequency domain imaging based on unpolarized light," Opt. Express **19**(2), 552–561 (2011).
40. B. H. Park, M. C. Pierce, B. Cense, and J. F. de Boer, "Jones matrix analysis for a polarization-sensitive optical coherence tomography system using fiber-optic components," Opt. Lett. **29**(21), 2512–2514 (2004).
41. A. S. Nam, I. Chico-Calero, and B. J. Vakoc, "Complex differential variance algorithm for optical coherence tomography angiography," Biomed. Opt. Express **5**(11), 3822–3832 (2014).
42. D. Lorenser, C. C. Singe, A. Curatolo, and D. D. Sampson, "Energy-efficient low-Fresnel-number Bessel beams and their application in optical coherence tomography," Opt. Lett. **39**(3), 548–551 (2014).
43. R. A. Leitgeb, L. Schmetterer, C. K. Hitzenberger, A. F. Fercher, F. Berisha, M. Wojtkowski, and T. Bajraszewski, "Real-time measurement of in vitro flow by Fourier-domain color Doppler optical coherence tomography," Opt. Lett. **29**(2), 171–173 (2004).
44. Y. Zhao, Z. Chen, C. Saxer, S. Xiang, J. F. de Boer, and J. S. Nelson, "Phase-resolved optical coherence tomography and optical Doppler tomography for imaging blood flow in human skin with fast scanning speed and high velocity sensitivity," Opt. Lett. **25**(2), 114–116 (2000).
45. R. A. Leitgeb, R. M. Werkmeister, C. Blatter, and L. Schmetterer, "Doppler optical coherence tomography," Prog. Retin. Eye Res. **41**, 26–43 (2014).

1. Introduction

Dermoscopy is a skin surface microscopic technique allowing specular reflection free observation of subsurface structures in the skin, and it has been widely employed by dermatologists for evaluating pigmented skin lesions including melanoma [1–4]. Usage of dermoscopy has been recently extended to diagnose non-pigmented skin lesions [5–7] as well as to monitor the treatment response in various skin lesions [8–10]. However, dermoscopy can visualize only superficial features in the skin with inaccurate depth information due to lack of 3D resolution.

Optical coherence tomography (OCT) is a 3D imaging technique based on low coherence interferometry, and provides depth-resolved information of tissue microstructure down to 1 - 2 mm with high-resolution and high-imaging speed [11]. Feasibility of OCT for skin examinations has been proven in various dermatological studies [12–15], and functional OCT techniques which can provide additional information such as polarization and vasculature have been developed. Polarization-sensitive OCT (PS-OCT) provides polarization properties of tissues such as birefringence, and it is useful for distinguishing lesions from normal tissues if the normal ones have polarization properties. PS-OCT has been applied to studying various organs including the skin [16–23]. Angiographic OCT based on flow characteristics provides additional vascular information within tissue, such as diameter, shape and distribution of blood vessels and their perfusion. Angiographic OCT has been applied to detecting abnormal vasculature of skin lesions such as port-wine stain (PWS) and basal cell carcinoma (BCC) [24–26].

Dermoscopy and OCT provide complementary information of the skin, and their combination can overcome the limitations of each method: Dermoscopy offers high-contrast superficial information and OCT offers accurate depth information of skin lesions. In previous studies, additional use of OCT to dermoscopy showed improvement of sensitivity and specificity in diagnosing non-pigmented BCC [27] and provided more precise pre-surgical margin of BCC [28]. Recently, a technical combination of dermoscopy and OCT using a dichroic mirror (DM) was demonstrated [29]. However, it did not utilize augmented functional OCT techniques such as polarization-sensitive and angiographic OCTs.

Suppressing specular reflection from the sample surface is another technical consideration in combining dermoscopy and OCT. Standard OCT using Gaussian beam in both illumination and detection suffers from specular reflection from the sample. This problem hinders the proper detection of sample reflection due to saturation, thus degrades image quality and

Biomedical Optics EXPRESS

makes polarization calculation difficult. In order to avoid this problem, samples are usually slanted from the normal of illumination beam. However, when combining dermoscopy and OCT, the sample slanting method may not be applicable due to the requirement of dermoscopy imaging. To reduce specular reflection without the sample slanting, dark-field OCT methods separating the illumination and detection light paths might be useful [30–34].

In this study, we developed dermoscopy guided multi-functional OCT (MF-OCT) which can simultaneously provide both high contrast superficial information and depth-resolved structural, birefringent, and vascular information of the skin. Dark-field configuration was adapted in MF-OCT to reduce specular reflection. System design and implementation were described and system performance was characterized. The newly developed dermoscopy guided MF-OCT was applied to several human skin lesions such as the scar and PWS together with the normal skin for demonstration.

2. Materials and methods

2.1 Instrumentation

A schematic of dermoscopy guided MF-OCT is shown in Fig. 1. The OCT setup is similar to the previously reported dark-field PS-OCT [31] and the sample arm was modified to use a 10x dermoscopy (DermLite DL3, 3Gen, USA) as the objective lens. The OCT light source was a wavelength swept source (SSOCT-1310, AXSUN Technologies) with the center wavelength of 1310 nm, bandwidth of 107 nm, sweeping speed of 50 kHz, 45.1% duty cycle, and imaging depth range of 6 mm in the air. Light from the source was split with 95:5 ratio: 95% of light went into the interferometry setup, and the remaining 5% was directed to a fiber Bragg grating (FBG, λ_0 = 1307.8 nm, Reflectivity = 97%, $\Delta\lambda$ = 0.08 nm, OE Land) to generate an external trigger signal for data acquisition. For PS-OCT imaging, a passive delay unit (PDU) was used to generate two orthogonal polarization states with 3 mm optical path length separation each other [31, 35, 36]. In the sample arm, light was collimated to 1.8 mm in diameter by a fiber collimator (HPUCO-13A-1300/1550-S-11AS, OZ optics). Beam profile of the collimated light was converted from Gaussian beam to Bessel beam by an axicon lens (AX255-C, Thorlabs) with 170° apex angle. The converted Bessel beam was relayed to the object plane by lenses (L1-L5) and the dermoscopy lens. L1-L4 (AC254-060-C, Thorlabs) and L5 (AC254-075-C, Thorlabs) were standard achromatic lenses with 60 mm and 75 mm focal lengths respectively. A dichroic mirror (DM, 1025dcspxr, Chroma) was placed in between L5 and dermoscopy to transmit visible dermoscopy light and to reflect OCT light. A 2D galvano scanning mirror (GVS 112/M, Thorlabs) was placed in between L3 and L4 to scan OCT beam in the sample plane. Illuminating Bessel beam was designed to have 8.6 μm central lobe size ($1/e^2$) and 1.7 mm depth of focus (DOF) in the sample with 0.117 numerical aperture (NA). Gaussian beam in the detection path was designed to have 0.025 NA, approximately 4.7 times smaller than that of Bessel beam for dark-field effect. Corresponding full width half maximum (FWHM) intensity of the focus in the sample was 19.4 μm in diameter and 2 times of Rayleigh range was 0.9 mm. Illumination and detection beam paths were separated by a right angle mirror (3mm Protected Gold Coated, N-BK7 Right Angle Mirror, Edmund optics) [31, 32]. Reflected light from both the reference and sample arms was combined and collected at a polarization diverse detection (PDD) setup. 1280 samples per each depth-scan were acquired with a digitizer (ATS9350, Alazar Technologies Inc.) by using the external trigger and clock signals from the Axsun light source. Part of data was processed and displayed in real time during acquisition. Acquired data was post-processed to generate intensity, PS, and angiographic OCT images by using MATLAB (Mathworks). Dispersion mismatch between the reference and sample arms was numerically corrected by pre-calibration data of a mirror sample [37, 38]. Polarization properties of the sample were obtained by Jones matrix-based analysis [39, 40], and the accumulated phase retardation with depth was calculated and displayed. Angiographic OCT images were obtained by a complex differential variance technique [41].

Biomedical Optics EXPRESS

For dermoscopy imaging, integrated visible light sources in the dermoscopy was used to illuminate samples in either cross-polarized or non-polarized modes. Light from the sample was collected by the dermoscopy lens, transmitted through the DM, relayed by a lens pair (L6, L7), and collected at a commercial smartphone (SHV-E330K, Samsung, Rep. of Korea) for imaging. L6 and L7 (AC254-075-A, Thorlabs) were standard achromatic lenses with 75 mm focal length. Resolution of dermoscopy was measured by imaging a USAF resolution target (R3L3S1N, Thorlabs), and was approximately 14.0 μm. An optical window at the distal end of dermoscopy was detachable and the imaging could be conducted in either the contact or non-contact modes.

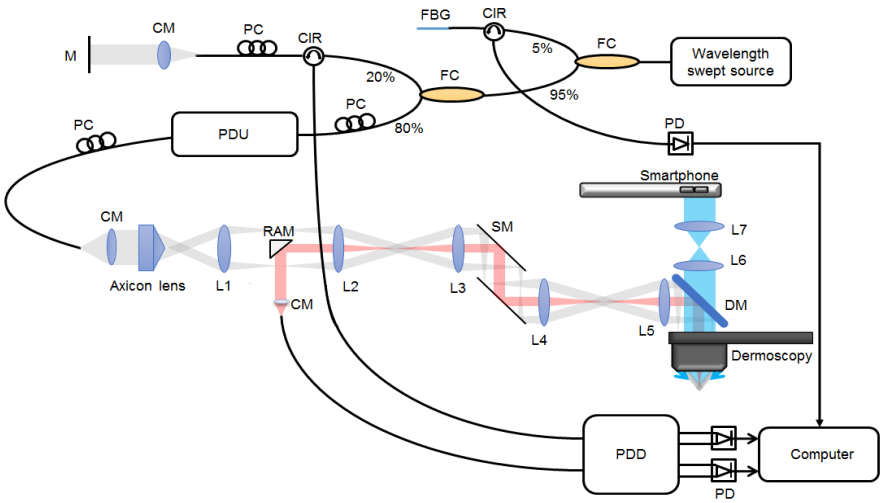

Fig. 1. System configuration of dermoscopy guided MF-OCT. Bessel beam illumination and Gaussian beam detection paths for dark-field effect are depicted in gray and red colors, respectively. PDU: passive delay unit, PC: polarization controller, FBG: fiber Bragg grating, CM: collimator, CIR: fiber circulator, FC: fiber coupler, PD: photodetector, PDD: polarization diverse detection, M: mirror, SM: scanning mirror, RAM: right angle mirror, DM: dichroic mirror, L1-L4: achromatic lens (f = 60 mm), L5-L7: achromatic lens (f = 75 mm).

2.2 System characterization

Lateral resolution of MF-OCT was measured by imaging microspheres (17134-15, 3 μm, Polysciences Inc.) embedded in 2% agarose gel, and the results are shown in Fig. 2. Since the microspheres were smaller than the expected lateral resolution, the microsphere images were equivalent to point spread functions (PSFs). An en-face intensity OCT image of microspheres at 300 μm deep from the surface is shown in Fig. 2(a). Microsphere images showed high intensity central lobes and surrounding side lobes, typical for Bessel beam. Enlarged images of a single microsphere at 200 μm, 350 μm, and 500 μm deep from the surface are shown in Figs. 2(b)-2(d) respectively. Average diameter of the central lobes was 9.4 ± 0.93 μm from 15 microsphere images. Axial resolution of MF-OCT was 8.94 ± 1.01 μm in the air by measuring the FWHM intensity of a mirror sample.

Sensitivity of the dark-field OCT cannot be measured by standard procedure using a mirror, due to different NAs of illuminating Bessel beam and detecting Gaussian beam. Therefore, the sensitivity of MF-OCT based on dark-field method was measured in comparison with a conventional OCT system whose sensitivity is known to be 103.2 dB. A turbid tissue phantom which had 0.4% TiO_2 in silicone by weight and the corresponding scattering coefficient of 8 mm^{-1} was imaged by MF-OCT and conventional OCT for comparison. Cross-sectional intensity OCT images of the tissue phantom acquired by the two OCT systems are shown in Figs. 3(a) and 3(b), and their mean intensity profiles with depth are shown in Fig. 3(c). The mean intensity profile of dermoscopy guided MF-OCT showed

Biomedical Optics EXPRESS

approximately 4 - 7 dB lower intensity levels than that of conventional OCT in the tissue phantom, which is typical for dark-field OCT. More discussion about the decreased sensitivity was given in the discussion section. In order to characterize the sensitivity of dermoscopy guided MF-OCT in the skin, the dorsum of human hand was imaged. Cross-sectional intensity OCT image and its mean intensity profile are shown in Figs. 3(d) and 3(e), respectively. The peak intensity inside the skin was approximately 19 dB above the noise level. The slope of intensity decay with depth was calculated by linear fitting, and it was approximately –0.020 dB/μm. These results were similar to a previous report [31].

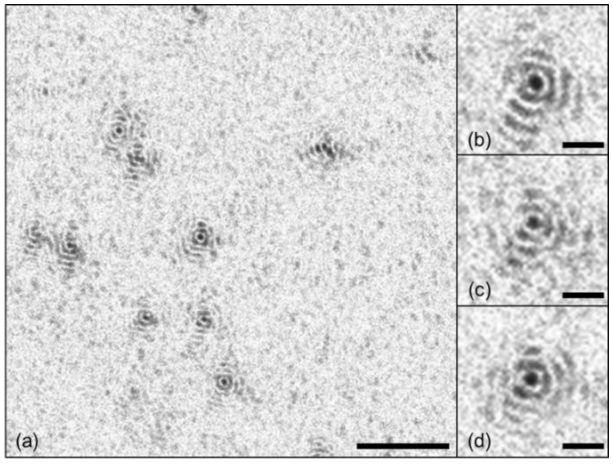

Fig. 2. (a) En-face intensity OCT images of microspheres (3 μm in diameter) at 300 μm deep from the surface. (b-d) Enlarged PSF images at 200 μm, 350 μm, and 500 μm deep from the surface. Scale bars are (a) 100 μm and (b-d) 20 μm.

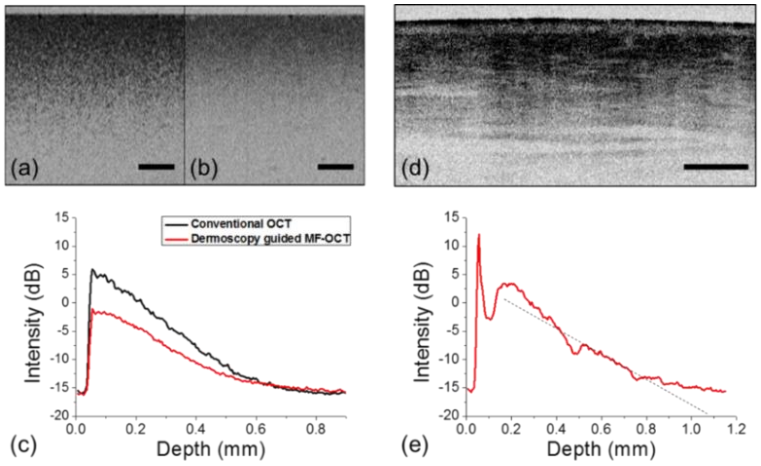

Fig. 3. Comparison between dermoscopy guided MF-OCT and conventional OCT in a tissue phantom and sensitivity analysis of dermoscopy guided MF-OCT in the human skin. (a, b) Cross-sectional intensity OCT images of a TiO_2 tissue phantom by dermoscopy guided MF-OCT and conventional OCT respectively. (c) Mean intensity profiles with depth of the two intensity OCT images in (a) and (b). (d) Cross-sectional intensity OCT image of the dorsum of human hand by dermoscopy guided MF-OCT. (e) Mean intensity profile with depth of the intensity OCT image in (d). All scale bars are 500 μm.

2.3 Experimental procedure

For human skin imaging, two human volunteers were recruited: a 31-year-old male Asian having congenital PWS on the right forearm, and a 27-year-old female Asian having a very

Biomedical Optics EXPRESS

old (16 years) whitish flat scar on the thumb side of dorsum of left hand. The study protocol was approved by the Institutional Review Board (IRB) of Pohang University of Science and Technology (PIRB-2016-A004). Prior to imaging, hair in the skin region of interest was trimmed with a razor blade to avoid artifacts in OCT imaging. Dermoscopy guided MF-OCT was applied in the contact mode by using the optical window in order to reduce motion artifacts. The skin was placed under the optical window, and water was added in between the window and skin to reduce reflection from the contacting interfaces. The illumination power onto the skin for OCT was 5 mW. 3D OCT imaging was conducted by recording cross-sectional B-scans in the x-z direction continuously with step-wise increment in the transverse y direction. For angiographic imaging, 10 B-scans were recorded at each cross-section and processed. For PS imaging, single B-scans were processed at each cross-section. 3D OCT images had the imaging field of view (FOV) of 2.8 mm x 2.8 mm x 2.25 mm in the x, y, and z directions consisting of 500 pixels x 500 pixels x 320 pixels. FOV of dermoscopy was 8 mm in diameter. The imaging time was approximately 50 s per volume.

3. Results

3.1 Normal skin

After characterization, dermoscopy guided MF-OCT was applied to the normal human skin as the control. Dermoscopy and MF-OCT images of the dorsum of human hand were acquired and the results are shown in Fig. 4. Dermoscopy image, cross-sectional intensity and PS-OCT images, and en-face angiographic OCT image of the normal skin are shown in Figs. 4(a)-4(d), respectively. Dermoscopy image in Fig. 4(a) shows detail superficial skin structures such as wrinkles and skin pores without specular reflection by cross-polarization illumination and imaging. MF-OCT images were acquired in a region of blue dashed box shown in Fig. 4(a). En-face angiographic OCT image was generated by maximum intensity projection (MIP) and depth-resolved color mapping. MIP was applied to 3D angiographic OCT images in the depth range from 100 μm to 400 μm deep from the surface, as indicated by two yellow dashed lines in intensity OCT image in Fig. 4(b). Intensity OCT image shows typical layered structure of the normal skin comprising the superficial weakly scattering epidermis, underneath highly scattering dermis, and some vertical shadows indicating blood vessels. PS-OCT image in Fig. 4(c) shows blue color in the epidermis and blue to red banding patterns in the dermis indicating birefringence due to collagen composition. The blue and red colors in PS-OCT image indicate 0° and 180° accumulated phase retardations from the surface, respectively. There are some vertical stripes in PS-OCT image, which are artifacts from calculation error of phase retardation. Angiographic OCT image in Fig. 4(d) shows typical vascular distribution in the skin: superficial capillary and deep large vessels.

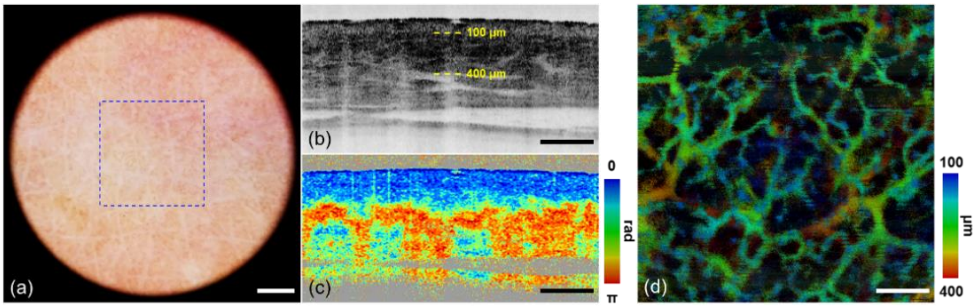

Fig. 4. Normal skin images by dermoscopy guided MF-OCT. (a) Dermoscopy image. (b) Intensity OCT and (c) PS-OCT images in the x-z plane (see Visualization 1). (d) MIP angiographic OCT image with depth resolved color mapping in the x-y plane. A blue dashed lined box indicates FOV of MF-OCT. Yellow-dashed lines indicate the depth range of angiographic OCT image. Scale bars are (a) 1 mm and (b-d) 500 μm.

Biomedical Optics EXPRESS

3.2 Scar

A whitish flat scar of the human volunteer was imaged by dermoscopy guided MF-OCT, and the results are shown in Fig. 5. Dermoscopy image, and intensity, PS, and angiographic OCT images of the scar are shown in Figs. 5(a), 5(b), 5(e), 5(c), 5(f), and 5(d), respectively. Intensity and PS-OCT images are shown in both the en-face and cross-sectional views, and white dashed lines in Figs. 5(b), 5(c) and 5(e), 5(f) indicate locations of the cross-sections and depth-sections, respectively. Two yellow dashed lines in the cross-sectional intensity OCT image indicate the depth range of en-face angiographic OCT image. En-face MIP angiographic OCT image is shown with depth resolved color mapping. Dermoscopy image in Fig. 5(a) shows the whitish scar out of the surrounding pinkish normal skin. The scar appears dark in intensity OCT images (Figs. 5(b) and 5(e)) due to strong light scattering. It appears as a red colored region out of the blue surrounding in en-face PS-OCT image (Fig. 5(c)), and as a rapidly color changing region in cross-sectional PS-OCT image (Fig. 5(f)) indicating strong birefringence. White arrows in Figs. 5(b) and 5(c) mark the scar region with strong light scattering and birefringence. Cross-sectional intensity and PS-OCT images in Figs. 5(e) and 5(f) show depth location of the scar just below the epidermis. Angiographic OCT image in Fig. 5(d) shows vasculature in the scar region and surrounding normal region. Less blood vessels are observed in the scar compared to the surrounding normal skin.

3.3 PWS

PWS and the contralateral control skin of the human volunteer were imaged by dermoscopy guided MF-OCT. Dermoscopy and MF-OCT images collected from the PWS and contralateral control are shown in Figs. 6(a)-6(d) and 6(e)-6(h), respectively, and they have same image configuration as the one of normal skin in Fig. 3. Intensity and PS-OCT images are shown in the cross-sectional view. En-face MIP angiographic OCT images are shown with depth resolved color mapping. Dermoscopy image of the PWS region in Fig. 6(a) shows more reddish skin color and some blood vessels compared to that of contralateral control in Fig. 6(e). Cross-sectional intensity OCT image of PWS in Fig. 6(b) shows more vertical shadows indicating blood vessels in the upper dermis than that of contralateral control in Fig. 6(f). PS-OCT image of PWS in Fig. 6(c) shows relatively slow accumulated phase retardation with depth compared to that of contralateral control in Fig. 6(g). Angiographic OCT image of PWS in Fig. 6(d) shows relatively thick superficial blood vessels, which is typical feature of PWS pathology. While those of the contralateral control in Fig. 6(h) shows thin superficial blood vessels and relatively thick ones in the deeper region. Both dermoscopy and MF-OCT show characteristic features of PWS, different from the normal skin.

4. Discussion

Dermoscopy guided MF-OCT was developed to provide both the superficial color image, and depth-resolved structural, birefringent, and vascular images of the skin simultaneously. Dermoscopy and MF-OCT were combined by using a DM, and the dermoscopy lens was used for both the OCT and dermoscopy imaging. Dark-field configuration was adapted to OCT for specular reflection free imaging. After its performance was characterized by imaging microspheres and scattering samples, dermoscopy guided MF-OCT was applied to several human skin lesions as well as the normal skin for demonstration. In the normal skin, dermoscopy guided MF-OCT simultaneously visualized detail superficial skin features and typical layered structure comprising epidermis, dermis, and composition of collagen and vasculature. In the scar, whitish superficial structure and depth-resolved highly scattering and birefringent structure were elucidated by dermoscopy guided MF-OCT. In the PWS, reddish superficial color and abnormally enlarged superficial blood vessels were observed. Features of these skin lesions were clearly visualized by dermoscopy guided MF-OCT.

Biomedical Optics EXPRESS

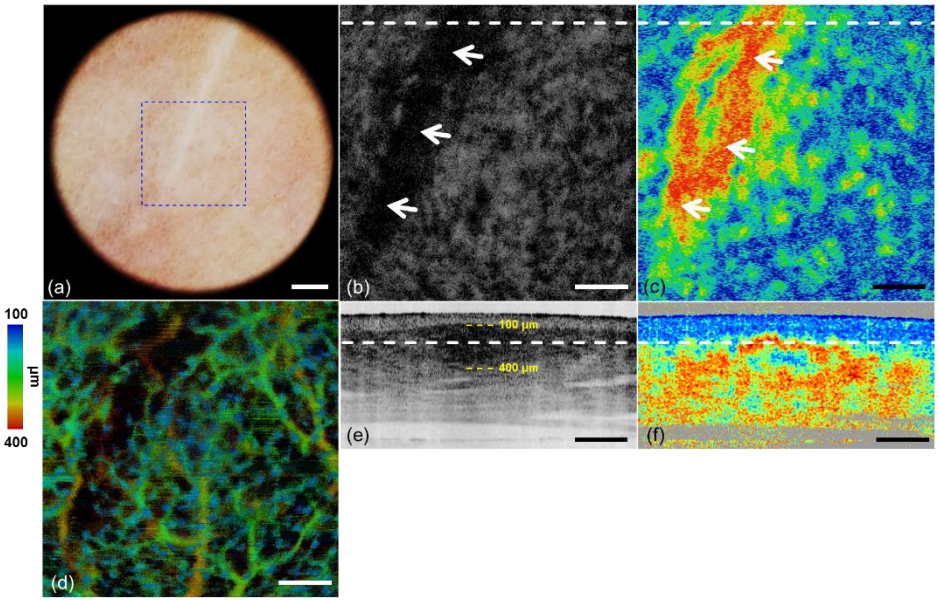

Fig. 5. Scar images by dermoscopy guided MF-OCT. (a) Dermoscopy image. (b, e) Intensity OCT and (c, f) PS-OCT images in the x-y and x-z plane respectively (see Visualization 2). (d) MIP angiographic OCT image with depth resolved color mapping in the x-y plane. A blue dashed lined box indicates FOV of MF-OCT. White dashed lines indicate locations of the cross-sections and depth-sections. White arrows indicate the highly scattering and birefringent regions in (b, c). Yellow dashed lines indicate the depth range of angiographic OCT image. Scale bars are (a) 1 mm and (b-f) 500 µm.

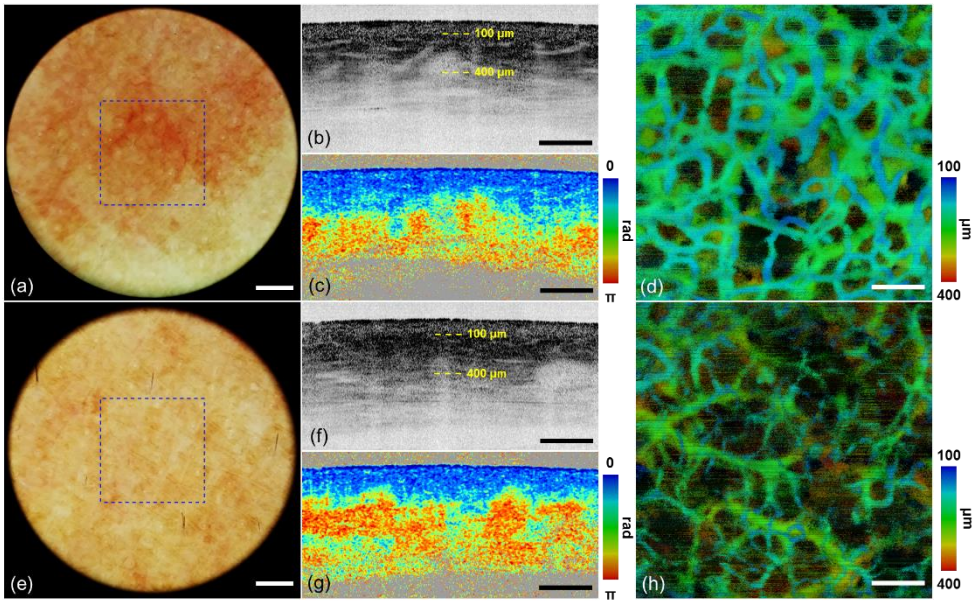

Fig. 6. Images of (a-d) PWS and (e-h) contralateral control by dermoscopy guided MF-OCT. (a, e) Dermoscopy images. (b, f) Intensity OCT and (c, g) PS-OCT images in the x-z plane (see Visualization 3 and Visualization 4). (d) MIP angiographic OCT image with depth resolved color mapping in the x-y plane. A blue dashed lined box indicates FOV of MF-OCT. Yellow-dashed lines indicate the depth ranges of angiographic OCT images. Scale bars are (a, e) 1 mm and (b-d, f-h) 500 µm.

Biomedical Optics EXPRESS

Sensitivity of dermoscopy guided MF-OCT was approximately 19 dB maximum in the human skin, which was 6 dB lower than that of conventional OCT using Gaussian beam in both the illumination and detection. However, sensitivity of the new dermoscopy guided MF-OCT was comparable with a previously reported dark-field PS-OCT using the same OCT engine [31]. The lower sensitivity of dermoscopy guided MF-OCT, compared to conventional OCT, was caused by several factors: (1) Bessel beam generated by the axicon lens tends to lose the source power due to their extensive side-lobes. Previous studies analyzed sensitivity penalties of Bessel beam based OCT resulting from the low power fraction in the central lobe [42]. Bessel beam with lower Fresnel number tends to have less sensitivity reduction. However, dermoscopy guided MF-OCT used Bessel beam having relatively high Fresnel number (N = 26.8) due to design limitation. (2) The 10x dermoscopy lens, which was used as the objective lens for MF-OCT, was not anti-reflection coated for the near-infrared OCT wavelength. (3) Imperfection at its conical tip of the axicon lens caused additional power loss. The conical tip in the axicon lens was not sharp enough so that some portion of light did not form Bessel beam after the axicon lens. Large sized Gaussian beam might be good in order to minimize the loss during beam profile conversion by the axicon lens.

In a next step, the system will be further improved and clinical studies will be conducted. As system improvement, Doppler OCT methods will be incorporated to obtain information on the blood flow rate in addition to the vasculature [43–45]. The blood flow rate will be more useful for skin disorders such as PWS or keloid scar because they have abnormal perfusion characteristics. Currently the sample arm of our system is quite bulky which limits the clinical applicability. Thus, a more compact sample arm needs to be designed which can be mounted on an articulated arm for flexible positioning of the system.

5. Conclusion

Dermoscopy guided MF-OCT which can visualize both the superficial features in color, and depth-resolved structural, birefringent, and vascular information of skin simultaneously, was developed. A commercial dermoscopy lens was used as the objective lens for both dermoscopy and MF-OCT imaging, and dark-field OCT configuration was adapted to reduce specular reflection. Dermoscopy guided MF-OCT was applied to several human skin lesions as well as the control for demonstration. It visualized typical features of the control skin, and abnormal features of the scar and PWS in both dermoscopy and MF-OCT images. Dermoscopy guided MF-OCT may be useful in both the diagnosis and treatment monitoring of skin lesions in clinical applications.

Funding

This research was supported in part by Engineering Research Center grant (No. 2011-0030075) and Korea-Sweden Research Cooperation Program (No. NRF-2014R1A2A1A12067510) of the National Research Foundation (NRF) funded by the Korean government (MEST), and Industrial Technology Innovation Program (No. 10048358) funded by the Ministry of Trade, Industry & Energy (MI, Korea).

Acknowledgments

We would like to thank Benjamin Vakoc (Center for Biomedical OCT Research and Translation, Grant Number P41EB015903) for generously providing us with the MATLAB angiographic analysis code and angiographic projection code.